Materials Research. 2025; 28: e20250329
DOI: https://doi.org/10.1590/1980-5373-MR-2025-0329

Effect of Heat Treatment on Microstructure and Performance of Laser Power Bed Fusion Processed Sc and C Element Modified Alsi10mg Alloy

Junyan Fang[a], Xinzhi Zhang[a], Xudong Zhao[a], Siyu Sun[a], Liubo Yang[c], Huaixue Li[b], Peng Liu[a]*

[a]*Shandong Jianzhu University, School of Materials Science and Engineering, 250101, Jinan, P. R. China.*
[b]*AVIC Manufacturing Technology Institute, Science and Technology on Power Beam Processes Laboratory, 100024, Beijing, P. R. China.*
[c]*BKSL Intelligent Technology Co., Ltd, Qingdao, P. R. China.*

Received: February 18, 2025; Revised: June 28, 2025; Accepted: August 03, 2025

This study investigated the laser powder bed fusion (LPBF) processed AlSi10Mg alloy modified by Sc and C elements, and explored the impact of heat treatment on its microstructure and properties. After solution treatment at 500°C for 3 h followed by aging at 150°C for 6 h, the grain size becomes smaller and more uniform, contributing to enhanced mechanical and corrosion properties. The self-corrosion potential (Ecorr) of alloy reaches -0.6536V, with a self-corrosion current (Icorr) of 3.528×10-7A/cm^2, indicating a significant boost in corrosion resistance. The alloy had the highest average hardness (HV 91.7) after a 3h solution treatment at 500°C and a 3h aging treatment at 200°C, which was attributed to the uniform dispersion of the Si phase in the α-Al matrix. Atomic force microscopy (AFM) results shew that the surface roughness is minimized after the 500°C+3h solution treatment and 150°C+6h aging treatment, with a Ra value of only 5.17nm. Neutral salt spray testing (SST) in simulated marine environments further validates that optimizing the heat treatment process effectively enhances the corrosion resistance of alloys. Overall, the combined modification of Sc and C, and heat treatment provides an effective approach to improve the performance of AlSi10Mg alloy.

Keyword: *LPBF, AlSi10Mg alloy, heat treatment, microstructure, corrosion resistance.*

1. Introduction

Aluminum alloy possesses several advantages, such as low density, high specific strength, and good thermal conductivity. As a result, it finds wide applications in machinery, building materials, sports equipment, aerospace, and other fields, particularly in the aerospace industry[1-3]. The increasing complexity of component shapes, thin walls, and the integration of structural performance are becoming an inevitable trend. However, the current technology for preparing aluminum alloy parts is unable to meet the requirements of the aforementioned industries. In recent years, Additive manufacturing has been proven to be a revolutionary technology for preparing metals and alloys, laser powder bed technology (LPBF)[4-7] has been able to achieve rapid and high-quality preparation of complex structures. However, compared to LPBF preparation of titanium alloy, stainless steel, nickel-based superalloys, and other materials, aluminum alloy faces challenges due to its low melting point, susceptibility to crack formation, and low plasticity during high temperature processing. The poor microstructural stability of crack-free Al alloys synthesized via additive manufacturing typically possesses poor heat resistance[8]. Research in this area started late and lacks maturity. A common issue with LPBF is the presence of metallurgical defects such as cracks, spheroidization, and porosity encountered by many materials[9-11]. Consequently, only a limited number of metals are suitable for printing parts with satisfactory density, desired microstructure, and strength[12-15]. According to some reports, the aluminum alloys that can be printed by LPBF technology are mainly limited to Al-Si eutectic alloys, such as AlSi12 and AlSi10Mg[16-18].

Processing aluminum alloys through LPBF, on the other hand, presents challenges. Aluminum powder itself light weight, poor flow characteristics, high reflectivity, high thermal conductivity, low laser absorption, easy oxidation. However, the successful application of LPBF in aluminum alloy processing is mainly achieved through the aluminum silicon (Al-Si) group casting alloy. Alloying aluminum with other metals helps overcome these initial challenges and enables efficient processing through LPBF. AlSi10Mg and AlSi12 alloys are the most commonly used aluminum alloys in LPBF systems because of their excellent castability, low shrinkage, and significant Al-Si eutectic composition[19]. AlSi10Mg is a subeutectic alloy in the Al-Si family, which has excellent solderability, hardenability and mechanical properties due to its proximity to the eutectic region in the Al-Si phase diagram[20,21]. Adding silicon to the alloy can reduce the melting point of the alloy, reduce shrinkage, and improve fluidity. The trace amount of Mg in Al-Si alloys facilitates heat treatment and improves their mechanical properties, making them suitable for use as structural components[22].

*e-mail: liupeng1286@163.com
Associate Editor: José Daniel Biasoli de Mello.
Editor-in-Chief: Luiz Antonio Pessan.

Particularly, the L-PBFed Al9Mg2Si alloy shows improved mechanical properties with the yield strength of 397 MPa and the elongation of 7.3%)[23].

As a common aluminum alloy, AlSi10Mg has been more and more widely used in aerospace, transportation, equipment manufacturing and other fields due to its high specific strength, low thermal expansion coefficient, wear resistance, corrosion resistance[24] and other excellent properties. However, poor secondary dendrites and coarse eutectic Si structures are inevitably formed in the traditional casting forming process. The as-cast AlSi10Mg exhibits typical Al-rich dendrite structure and eutectic phase, accompanied by Fe-rich intermetallic compounds[25]. Recently, there have been attempts to use additive manufacturing (AM) techniques to prepare high-performance materials. Among them, LPBF technology can effectively reduce grain size and internal defects[26,27]. AlSi10Mg formed by LPBF has a saturated Si network structure precipitated along the α-Al grain boundary, showing fine grains[28]. However, rapid melting and solidification in the LPBF process, as well as cyclic heating and cooling, often produce residual stresses and micro cracks that reduce the toughness of AlSi10Mg[29-31]. In order to alleviate this problem, post-heat treatment is used to change its microstructure to improve its performance.

When preparing AlSi10Mg alloy using laser powder bed fusion technology, the addition of Sc and C elements can significantly enhance the comprehensive properties of the alloy through synergistic modification. Sc can form fine and dispersed Al_3Sc strengthening phases in the alloy, which can greatly increase the strength and hardness of the alloy through precipitation strengthening mechanism, and also improve the toughness of the material by refining the grains. C can form Al_4C_3 strengthening phases with Al, which can further reinforce the matrix and optimize the fluidity of the molten pool, reducing the formation of defects such as pores and cracks during laser printing. Moreover, the combined addition of Sc and C can promote the uniform distribution of strengthening phases under rapid solidification conditions, and synergistically exert the effects of fine-grain strengthening and second-phase strengthening. This allows the AlSi10Mg alloy to maintain good formability while achieving higher tensile strength, yield strength, and fatigue resistance, making it particularly suitable for the manufacturing of high-end components with strict mechanical property requirements. Extensive research has been done to understand the importance of post-production heat treatment of LPBF aluminum components[32]. Adjust the temperature and time of LPBF aluminum alloy heat treatment, such as the T6 process. This approach is designed to optimize its performance. Stress relief can also be obtained for aluminum alloys under heat treatment conditions. Tensile residual stress is unavoidable in additive manufacturing surfaces and delamination processes. The sample undergoes rapid heating and sudden cooling, resulting in tensile residual stress[33]. Stress relief helps to reduce these residual stresses and improve mechanical properties. At present, the research focus of AlSi10Mg alloy formed by LPBF is mainly on its mechanical properties. In addition to this, corrosion performance is another key issue for the use of LPBF formed AlSi10Mg in corrosive environments[34,35].

In this study, EP-M650 four-laser large-size metal printer was used to prepare AlSi10Mg samples, and high C and low Sc alloy components were added. The addition of C and Sc elements in AlSi10Mg alloy prepared by LPBF is aimed at improving the strength, thermal stability and corrosion resistance of the alloy. In addition, the properties of the alloy were optimized by solution treatment combined with aging strengthening process at different temperatures and different times, and the excellent microstructure, corrosion resistance and mechanical properties before and after heat treatment were studied. These results will contribute to the development of an alloy with reduced thermal crack sensitivity, improved corrosion resistance and improved strength as a potential reference for the preparation of AlSi10Mg alloys by LPBF.

2. Materials and Methods

In this study, EP-M650 four-laser large-size metal printer was used to prepare AlSi10Mg samples. The powder material used (AlSi10Mg) is spherical powder. The diameter of the powder is 15~40μm, and the chemical composition is shown in Table 1. LPBF manufacturing scanning strategy diagram is shown in Figure 1. All samples are printed on a 316L stainless steel substrate with a preheating temperature of 80°C. Throughout the forming process, high purity argon acts as the protective atmosphere of the forming chamber, maintaining a consistent directional scanning strategy within each layer and forming under the condition of 17° rotation between layers. Detailed process parameters and sample numbers are shown in Table 2. Sample No. 1 was deposited, and samples No. 2 to No. 4 were treated by solution and aging respectively. The solution treatment temperature is 500°C, the duration is 3h, the aging treatment temperature is 150°C or 200°C, the duration is 3h or 6h. All heat treatment processes are water quenching cooling, which is convenient for rapid cooling and higher mechanical properties.

The AlSi10Mg alloy sample prepared by LPBF was analyzed by optical microscope (OM), Nikon Epiphot 300U, field emission scanning electron microscope (SEM) and energy dispersive spectrometer (EDS). The hardness of the material was measured by digital display automatic rotary hardness tester (HFS-1000). The corrosion resistance of the material was characterized by Atomic force microscope (AFM), electrochemical workstation (CHI760E) and neutral salt spray test chamber (GW-60). The ratio of metallographic corrosion solution is HF: HCL: HNO_3: H_2O= 1:1.5:2.5:95. When measuring the hardness, the load is 0.3kg and the loading time is 10 seconds. The CHI760E electrochemical workstation uses 3.5wt% NaCl corrosion solution. The EIS curve frequency parameter is set to 10~10^6Hz, and the Tafel curve scanning

Table 1. Chemical composition of AlSi10Mg alloy powder for LPBF process (wt.%).

Elements	Al	Si	Mg	C	Sc	Impurity
wt%	Bal.	0.10	0.30	0.32	0.01	≤0.05

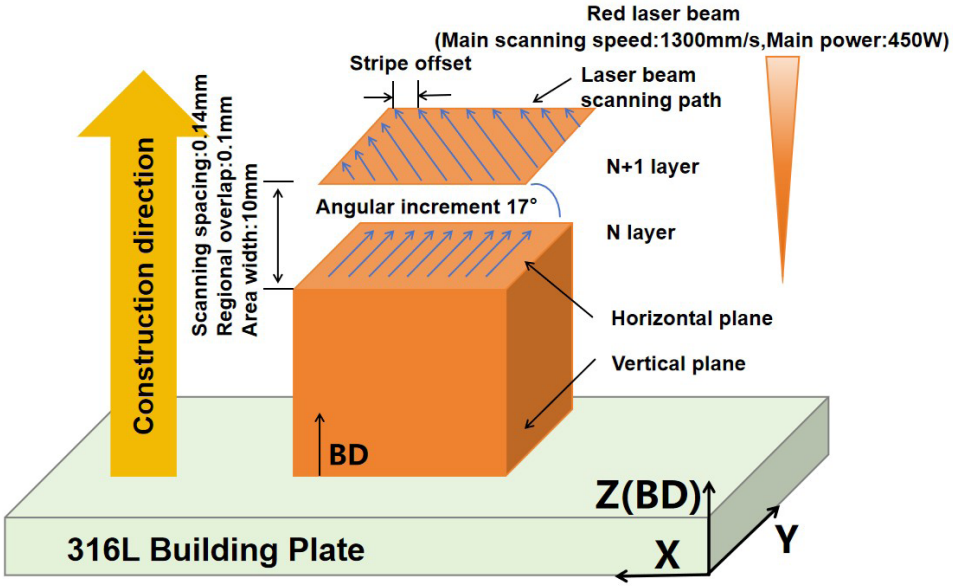

Figure 1. Scanning strategy diagram of AlSi10Mg alloy as-received.

Table 2. Parameters of AlSi10Mg alloy by LPBF under different heat treatment processes.

Number	Solution treatment temperature /°C	Solution treatment time /h	Solution treatment cooling method	Aging treatment temperature /°C	Aging treatment time /h	Aging treatment cooling method
1	as-received					
2	500	3	Water quenching	-	-	-
3	500	3	Water quenching	150	6	Water quenching
4	500	3	Water quenching	200	3	Water quenching

rate parameter is set to 0.01V/s. The acceleration voltage of the electron gun in the SUPRATM55 thermal field emission scanning electron microscope is set to 5~10KV. GYW-60 salt spray test chamber temperature is 35°C±5°C, NaCl solution mass fraction is 5%, pH range is 6.5~7.2, continuous spray.

3. Results and Analysis

3.1. AFM surface characterization

To quantify surface roughness, Ra (mean roughness) and Rq (root-mean-square roughness) are selected as descriptors of surface heterogeneity. Specifically: (1) Ra represents the average deviation of the surface profile relative to its mean, representing the flatness or roughness in the horizontal (or vertical) direction. The smaller the Ra value is, the smoother the surface is. (2) Rq is the root-mean-square value of surface roughness, reflecting the overall irregularity of surface profile fluctuations in the horizontal (or vertical) direction. The larger the Rq value, the more irregular the surface. The roughness results showed the unique characteristics of the sample, indicating that the Ra value and Rq value of the sample obtained after solution treatment at 500°C for 3h and aging treatment at 150°C for 6h were the lowest, as shown in Figure 2c. In this case, the average Ra value was 5.17nm and the average Rq was 7.15nm, indicating that the surface was smoother.

Through the analysis of AFM imaging results, the surface smoothness between different samples can be compared. The smoother the surface, the lower the roughness. In addition, select areas with large imaging differences after different heat treatment, and check the height difference between peaks and valleys, the smaller the difference means the more uniform, thereby reducing the overall roughness. It is shown that the surface growth of the pattern after heat treatment does not follow a uniform roughness pattern. This change is directly related to the heat treatment process of the pattern, and the detailed analysis is combined with the microstructure evolution discussed below.

3.2. Microstructural characterization

Figure 3 shows the microstructure of AlSi10Mg alloy samples prepared by LPBF process under different heat treatment parameters. The original microstructure of AlSi10Mg alloy is mainly composed of aluminum matrix, silicon phase, magnesium phase and other phases depending on other trace elements. After the solid solution treatment, the silicon and magnesium in the alloy will be partially dissolved in the aluminum matrix, forming a more uniform solid solution. During the aging treatment, Mg_2Si will precipitate and form fine precipitated phases, which will significantly improve the strength of the alloy. After aging treatment, the silicon phase may change and become finer and more evenly distributed. The strength and hardness of the aluminum matrix will be

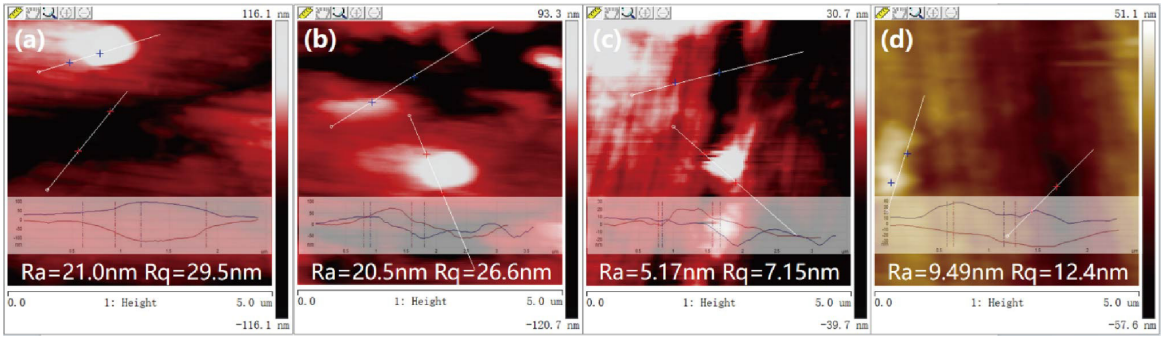

Figure 2. AFM 2D images of AlSi10Mg alloy by LPBF under different heat treatment processes. (a) as-received; (b) Solution treatment at 500°C for 3h; (c) Solution treatment at 500°C for 3h+ aging treatment at 150°C for 6h; (d) Solution treatment at 500°C for 3h+ aging treatment at 200°C for 3h.

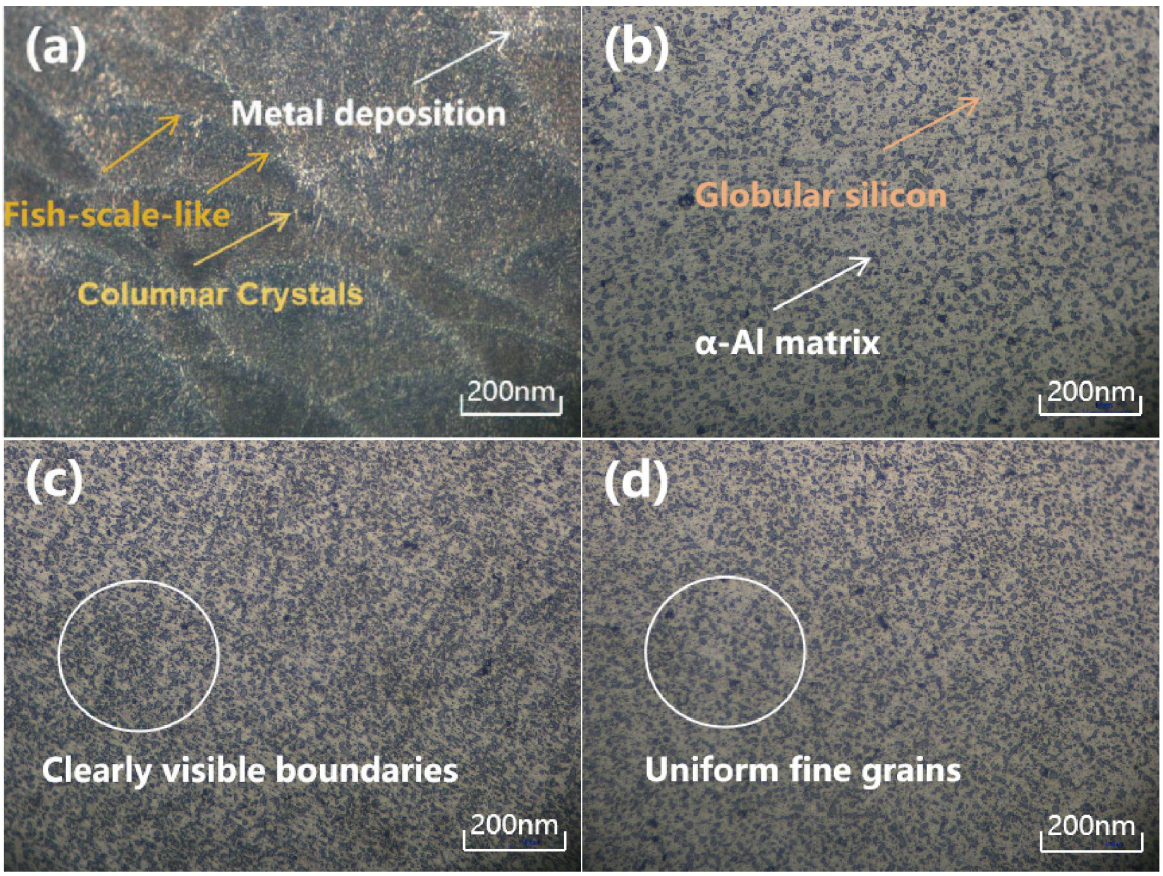

Figure 3. Microstructure of AlSi10Mg alloy by LPBF under different heat treatment processes. (a) as-received; (b) Solution treatment at 500°C for 3h; (c) Solution treatment at 500°C for 3h+ aging treatment at 150°C for 6h; (d) Solution treatment at 500°C for 3h+ aging treatment at 200°C for 3h.

increased, and the microstructure will be denser. Figure 3a shows a distinct weld pass, which is mainly due to metal deposition between welds during the LPBF process. The laser melting speed in the LPBF process is very fast, the metal powder melts and solidifies rapidly under the laser irradiation, the energy of the laser beam is concentrated in a small area, resulting in local temperature increase, while the surrounding area is relatively cold, and the melting and solidification of each layer will have a thermal effect on the underlying material, which may lead to the recrystallization or phase transition of the underlying material. These factors can lead to the non-uniform growth of grains, resulting in the formation of wave-like microstructure.

After solid solution at 500°C for 3h, the AlSi10Mg alloy (Figure 3b) has uniform and fine grains, and the α-Al matrix and Si phase are obvious. The silicon phase usually

appears as white particles or a network structure within the Al matrix. Structurally, the prominent existence of α-Al matrix and Si phase can be attributed to the rapid cooling in the LPBF process[36], which leads to the preferential formation of α-Al nuclei due to high nucleation density, which hinders the further growth of grains. As a result, Si atoms are pushed towards the solid-liquid interface, causing the Si concentration in the remaining liquid metal to increase until a eutectic composition is reached. Subsequently, a continuous network structure (α-Al+Si) is formed at the α-Al grain boundary by eutectic transition[37]. The microstructure distribution of AlSi10Mg alloy after solid solution at 500°C for 3h and aging at 150°C for 6h is shown in Figure 3c. The microstructure distribution of AlSi10Mg alloy after solution at 500°C for 3h and aging at 200°C for 3h is shown in Figure 3d. The results show that the grain size is further refined and the grain distribution uniformity is improved after solution treatment. This indicates that during the aging process[38], the Si phase has a finer particle size and a more uniform dispersion after spheroidization in the α-Al matrix. Combined with the above surface roughness analysis, the results show that the surface roughness of AlSi10Mg alloy is smaller after solid solution at 500°C for 3h and aging at 150°C for 6h, which is directly related to the smaller and uniform grain size obtained after solid solution treatment and aging treatment and the precipitation of more dispersed and uniform phase. And suitable aging treatment temperature and time control is also crucial.

3.3. SEM and EDS analysis

To know deeper insights into the effect of heat treatment on the surface microstructural transformation of AlSi10Mg alloy fabricated by LPBF, a scanning electron microscopy (SEM) with energy dispersive spectroscopy (EDS) was employed for observation and analysis. The microstructure of the alloy as observed through SEM is presented in Figure 4, while Figure 5 displays the EDS images of typical precipitates on the alloy surface. Table 3 provides the EDS analysis results of typical precipitates found on the surface of the alloy.

The experimental results show that the primary phase of AlSi10Mg alloy is composed of α-Al matrix phase and Si phase (see Figure 4a). The Si phase is reticular or fibrous and has a very fine layered eutectic structure. After solution at 500°C for 3h and aging at 150°C for 6h, the eutectic Si in the alloy began to spheroidize, resulting in the dissolution of fibrous eutectic Si. In addition, Si aggregates and transforms into blocky or coarse strip form. During aging treatment, due to low temperature, Si elements in the alloy precipitate to form nanoscale Si particles. These precipitates can act as barriers to grain growth, thus affecting the hardness and strength of the material. At the same time, some intermetallic compounds and segregation hardening phases are also

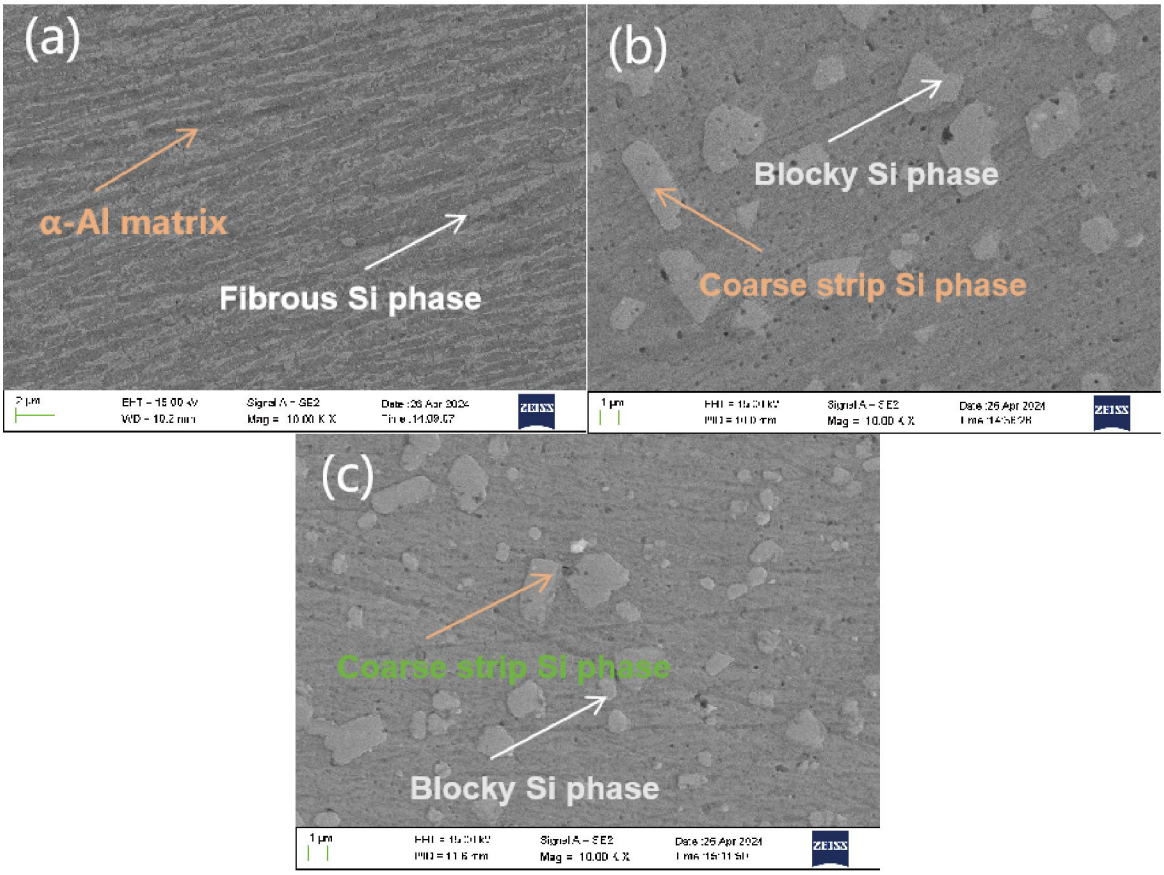

Figure 4. SEM image of AlSi10Mg alloy by LPBF under different heat treatment processes. (a) as-received; (b) Solution treatment at 500°C for 3h+ aging treatment at 150°C for 6h; (c) Solution treatment at 500°C for 3h+ aging treatment at 200°C for 3h.

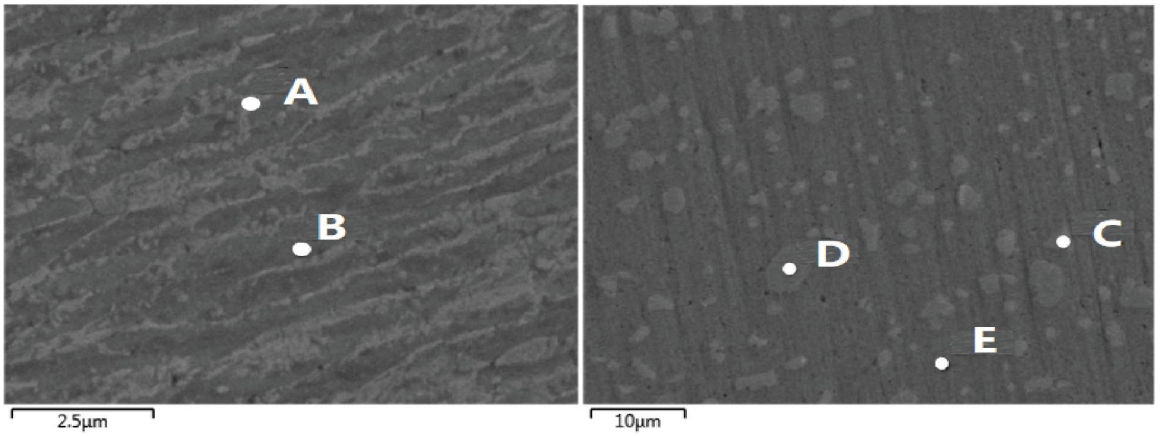

Figure 5. The EDS elemental analysis sampling diagram of AlSi10Mg alloy by LPBF under different heat treatment processes.

Table 3. EDS results of specific element proportion (wt.%).

Test Points	Elements				
	C	Mg	Al	Si	Sc
A	34.40	0.29	58.70	6.61	-
B	32.89	0.29	60.34	6.41	0.08
C	34.54	-	10.86	54.48	0.11
D	30.88	0.11	8.31	60.67	0.03
E	29	0.25	69.74	0.69	0.32

dissolved, resulting in significant microstructure changes. Remarkably, the previously very fine layered eutectic structure is now fully homogenized (see Figure 4b). Brandl et al.[39] also reported similar results after solution at 525°C for 6h and aging at 165°C for 7h. However, a large amount of Si phase structure is further precipitated. With the increase of solution temperature, the Si phase is dispersed more evenly in the α-Al matrix after spheroidization, and the grain size is finer and the distribution is more uniform (see Figure 4c).

According to Table 3, the majority elements labeled A and B (see Figure 5a) are Al elements, followed by C elements. Moreover, there is minimal disparity in the atomic content of Mg elements between the matrix and tissue in the deposition state. Additionally, a small quantity of Si element is present, while the matrix does not contain Sc element, indicating limited aggregation of Si phases in the deposited aluminum alloy. Following solid solution and aging treatment, Si phases began to spheroidize and irregularly aggregate into extensive homogenization[37]. The observed aggregated Si phases labeled C and D in Figure 5b, along with EDS analysis results shown in Table 3 indicate a substantial increase in Si element content within the aggregated matrix compared to that within the deposited matrix. This is consistent with previous microstructural analysis. Simultaneously, C element concentration within the aggregated structure is relatively lower than that within the deposited structure, suggesting reduction of C element alongside an increase in Si element during heat treatment processes.

Therefore, the above distribution results of alloying elements under different heat treatment conditions can be attributed to the following reasons: (1) During the heat treatment process, AlSi10Mg alloy typically undergoes solid solution treatment, wherein the alloy is heated to a specific temperature to dissolve Si, Mg, and other elements, forming a supersaturated solid solution. In this process, the C element may dissolve into the aluminum matrix, thereby reducing its content in the aggregated structure; (2) Subsequent to solid solution treatment, aging treatment may be applied to AlSi10Mg alloy, involving heating at a lower temperature to facilitate the formation of precipitated phases (such as Si and Mg_2Si)[40]. Throughout this procedure, C element may precipitate or redistribute due to decreased solubility in the aluminum matrix, leading to a relative decrease in aggregate structure; (3) The increase in temperature during heat treatment can result in precipitation of Si element as larger particles within the alloy, altering its microstructure. This structural modification could lead to changes in C element distribution and consequently cause a relative decrease in aggregate structures.

In addition, the EDS elemental analysis at point E (see Figure 5E), exhibit higher concentrations of Mg and Al elements, lower levels of C elements, and significantly reduced amounts of Si elements (see Table 3). This is attributed to the partial dissolution and fragmentation of the original continuous Si phase in the eutectic during heat treatment, leading to morphologic changes characterized by predominantly regular large particles and some smaller particles with more rounded shapes. These particles are evenly dispersed within the α-Al matrix. This phenomenon is primarily a result of accelerated atom diffusion, particularly that of Si atoms, at elevated heat treatment temperatures. In the LPBF process, due to rapid cooling rates, the diffusion of Si element lags

behind, resulting in a supersaturated solid solution formation in α-Al which further enhances alloy strength[41].

At the same time, Si and Mg_2Si precipitate in the Al matrix, serving as the primary secondary phases in LPBF-prepared AlSi10Mg alloy. This phenomenon contributes to enhancing the mechanical properties of the alloy. Despite C not being the principal alloying element in AlSi10Mg alloy, its presence as an impurity or trace alloying element can exert influence on the properties of the alloy. During heat treatment, precipitation of C may occur due to its low solubility in the Al matrix, thereby affecting both microstructure and properties of the alloy. In general, Sc, functioning as a micro-alloyed element, has potential to form high-strength scandium carbide or scandium nitride particles with Al[42]. These particles can serve as a means for precipitation strengthening and contribute to improving both yield strength and tensile strength of the alloy. Additionally, the element Sc has been found to enhance corrosion resistance of this particular alloy.

3.4. Hardness distribution

Based on the above analysis, there has been a noticeable alteration in the microstructure of the alloy. Hence, it holds significant importance to comprehend the correlation between microstructural changes and heat treatment processes through an examination of the hardness distribution in alloys. The depiction of hardness distribution on the surface of the alloy is illustrated in Figure 6 and Figure 7. The effect of temperature and time of aging treatment on the hardness of the alloy was systematically discussed in this paper. The results show that the appropriate aging treatment is an important factor to determine the hardness of the alloy. Among them, the average hardness of the deposited state is HV 143.6 (see Figure 6).

After heat treatment at 500°C for 3h, the average hardness reached HV 88.4 (see Figure 7). After heat treatment at 500°C for 3h and aging treatment at 150°C for 6h, the average hardness of the alloy decreased to HV 78.6 (see Figure 7). At the same time, by adjusting the solution treatment condition to 200°C and holding for 3h, the average hardness of the alloy was significantly increased to HV 91.7 (see Figure 7). This observation highlights a key point: even with extended aging time, at low aging temperatures, the precipitates inside the alloy may under nucleate and grow, limiting the hardness improvement. These data highlight the important role of temperature and time in adjusting alloy hardness during solution treatment and aging treatment. The proper heat treatment process not only helps to effectively nucleate and grow the precipitated phase, but also maintains a fine and uniform structure, which is the key to improving the hardness of the alloy[43].

Additionally, aging treatment subsequent to solution treatment exerted a notable influence on the alloy hardness. For instance, with a heat treatment process involving solid solution treatment at 500°C for 3h followed by aging treatment at 150°C for 6h, the average hardness was HV 78.6. However, changing to aging treatment at 200°C for 3h under identical solid solution conditions resulted in a significant increase in average hardness to HV91.7. This indicates that even though the aging duration is prolonged, a lower aging temperature may hinder sufficient nucleation of precipitated phases within the alloy, resulting in a hardness value lower than that of the alloy aged at a higher temperature. Furthermore, the research also revealed that at a solution temperature of 535°C, the microstructure of AlSi10Mg alloy underwent changes with increasing solution time, leading to accumulation and growth of eutectic Si phase. Consequently, the hardness of the alloy rapidly decreased from approximately HV 119 before solution to eventually stabilize at around HV 57[44]. This demonstrates that prolonged solution time leads to an increase in eutectic Si phase size and reduced density, consequently lowering the hardness of the alloy. It is found that the enhanced mechanical properties are mainly attributed to the newly formed ultrafine in-situ Mg_2Si particles[45].

In summary, solid solution treatment at 500°C for 3h followed by aging treatment at 200°C for an additional 3h significantly enhanced the nucleation and growth of the precipitated phase. This process maintains a fine and uniform microstructure within the alloy, thereby increasing its hardness. These findings underscore the critical influence of temperature and duration during both solution treatment

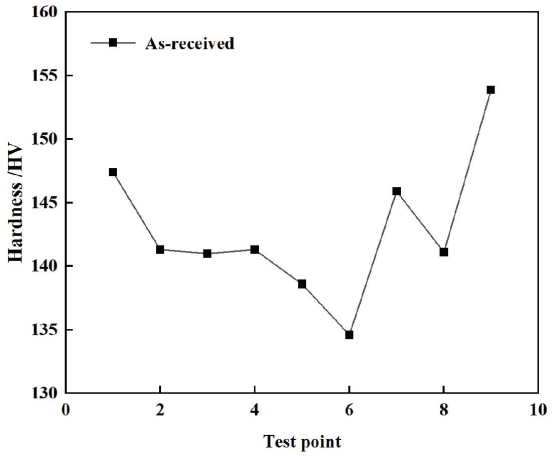

Figure 6. Hardness distribution of AlSi10Mg alloy as-received.

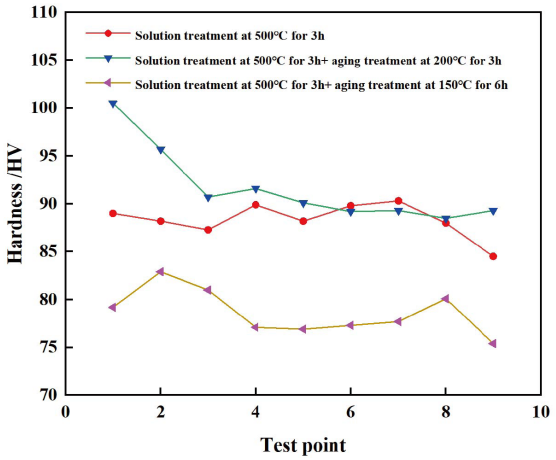

Figure 7. Hardness distribution of AlSi10Mg alloy by LPBF under different heat treatment processes.

and aging on the hardness of AlSi10Mg alloy. Subsequently, we examined the corrosion resistance of aluminum alloys subjected to various processing conditions.

3.5. Corrosion resistance

The Origin analysis and CHI760E series electrochemical measuring instruments were utilized to analyze the Tafel polarization curves of samples No. 1 to No. 4 subjected to various heat treatment processes (see Figure 8). The resulting data provided insights into the self-corrosion current density and potential. Analysis of the self-corrosion potential revealed that sample No. 3 exhibited the most positive potential, followed by samples No. 4, No. 1, and finally, sample No. 2 with the most negative potential. The relationship of self-corrosion current was observed as follows: sample No. 4 > sample No.1 > sample No .2 >sample No. 3, indicating that the self-corrosion current of sample No.3 is minimal in comparison. Table 4 presents Tafel fitting data for different heat treatment processes. Finally, it can be concluded that Sample No .3 demonstrates superior corrosion resistance owing to its solid solution treatment at 500°C for 3h combined with aging treatment at150°C for 6h.

The electrochemical impedance spectroscopy (EIS) was conducted using the CHI760E series electrochemical measuring instrument, and the resulting impedance diagram is presented in Figure 9. Analysis of the impedance fitting diagram in Figure 9 reveals that the low-frequency region exhibits a significantly larger impedance arc for sample No. 3 compared to other heat treatment processes. Specifically, sample No. 3 underwent a solid solution treatment at 500°C for 3h followed by aging treatment at 150°C for 6h, which likely facilitated the formation of a more compact and protective oxide film on the alloy surface, thereby enhancing its corrosion resistance. In EIS results, the low-frequency impedance arc reflects the charge transfer step of the corrosion process, encompassing charge transfer at the metal-electrolyte interface and potential electrochemical reactions. Consequently, a greater low-frequency impedance arc indicates a higher energy barrier in this process, often associated with superior corrosion resistance of alloys. In summary, EIS results demonstrate that sample No. 3 exhibits enhanced electrochemical stability and corrosion resistance following specific heat treatments. Thus subsequent experimental discussions will focus on solid solution treatment and aging treatment.

In order to further investigate the corrosion resistance of AlSi10Mg alloy through heat treatment, the corrosion behavior of AlSi10Mg alloy in a simulated marine environment was assessed using neutral salt spray test (SST). In accordance with china standard GB/T10125-2012 “Salt Spray Test for Artificial Atmosphere Corrosion Test”(China), the corrosion of samples after salt spray test was evaluated. During the 72 hour neutral salt spray test of AlSi10Mg alloy, different heat treatment processes exhibited significant effects on its corrosion resistance.

The surface of the untreated alloy displayed continuous white rust and black spots, possibly attributed to uneven formation of corrosion products and pitting phenomena on the alloy surface (see Figure 10a). Upon treatment at 500°C for 3h, the alloy exhibited a substantial presence of white rust and severe pitting, along with numerous black spots on its surface (see Figure 10b), indicating inadequate corrosion resistance. In contrast, following a heat treatment process involving solid solution treatment at 500°C for 3h followed

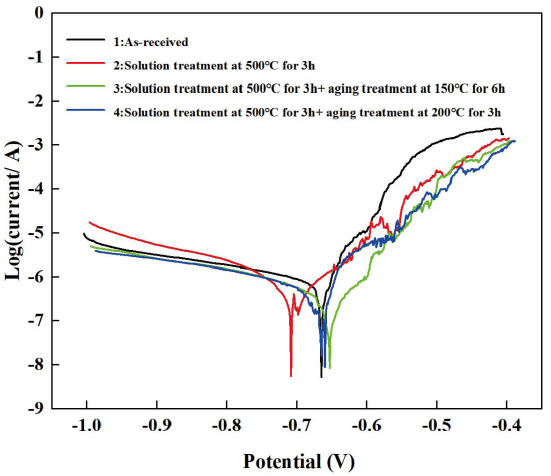

Figure 8. Tafel curves of AlSi10Mg alloy by LPBF under different heat treatment processes.

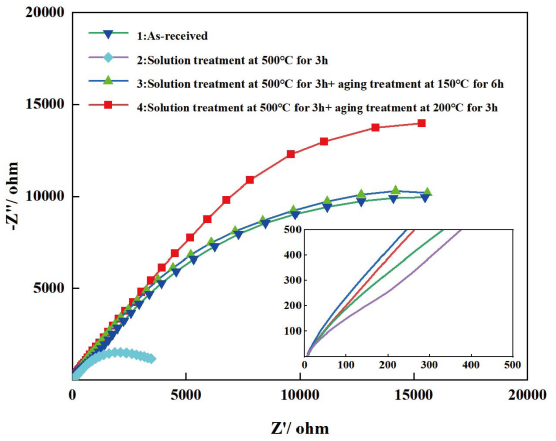

Figure 9. Impedance diagram (EIS) of AlSi10Mg alloy by LPBF under different heat treatment processes.

Table 4. Tafel fitting data of AlSi10Mg alloy by LPBF under different heat treatment processes.

Samples	Self-etching current icorr(A/cm^2)	Self-corrosion potential Ecorr(V)
1	8.117×10^{-7}	-0.6639
2	6.579×10^{-7}	-0.7079
3	3.528×10^{-7}	-0.6536
4	9.748×10^{-7}	-0.6603

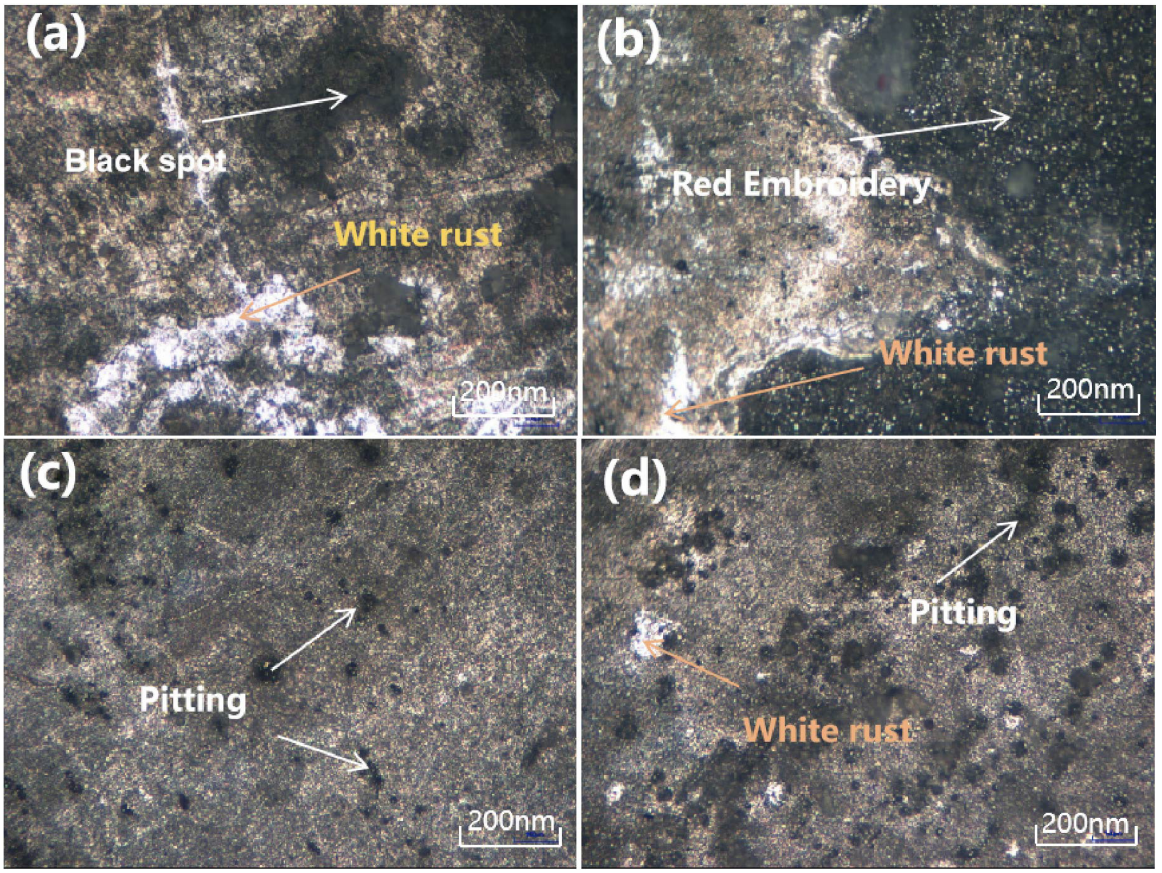

Figure 10. Salt spray test (72h) of AlSi10Mg alloy by LPBF under different heat treatment processes. (a) as-received; (b) Solution treatment at 500°C for 3h+ aging treatment at 150°C for 6h; (c) Solution treatment at 500°C for 3h+ aging treatment at 200°C for 3h.

by aging treatment at 200°C for 3h, the alloy displayed reduced occurrences of black spots and white rust on its surface (see Figure 10d), suggesting an enhancement in its corrosion resistance. Notably, when subjected to a heat treatment process comprising solid solution treatment at 500°C for 3h followed by aging treatment at 150°C for 6h, the alloy demonstrated minimal surface corrosion, characterized only by limited instances of black aggregation pitting and negligible white rust (see Figure 10c), signifying superior corrosion resistance.

These findings underscore that appropriate heat treatments can effectively enhance the corrosion resistance of AlSi10Mg alloy, particularly through a combination of solution treatment at 500°C for 3h followed by aging treatment at 150°C for 6h. This specific thermal processing regimen may facilitate the development of a denser and more protective oxide film on the alloy's surface, thereby augmenting its overall corrosion resistance.

4. Conclusion

The microstructures and properties of AlSi10Mg alloy fabricated by LPBF under various heat treatment processes were systematically investigated. The results revealed that the microstructures, hardness and corrosion resistance of AlSi10Mg alloy exhibited distinct variations in response to different heat treatment processes.

(1) When the solution at 500°C for 3h and aging at 150°C for 6h was used, the AlSi10Mg alloy fabricated by LPBF has the smallest surface roughness. The Ra value is only 5.17nm, and has the highest corrosion resistance. And its average hardness is also the lowest, with an average hardness of HV 78.6.

(2) With the increase of aging treatment temperature, the hardness of AlSi10Mg alloy increased significantly. After solution treatment at 500°C for 3h and aging treatment at 200°C for 3h, the average hardness of AlSi10mg alloy was the highest (HV 91.7). At this time, the effect of spheroidization results in more uniform dispersion of Si phase in α-Al matrix, smaller grain size, and higher hardness and corrosion resistance.

(3) After undergoing solution treatment at 500°C for 3h and aging treatment at 150°C for 6h, AlSi10Mg alloy fabricated by LPBF exhibited a reduced and more uniform grain size. And the self-corrosion potential (Ecorr) of the alloys was measured to be -0.6536V, with a corresponding self-corrosion current (icorr) of 3.528×10-7A/cm^2.

(4) The results from the 72 hour neutral salt spray test demonstrate that properly heat-treated alloys exhibit superior corrosion resistance. Therefore, the low-temperature, short-time aging heat treatment is an effective method for optimizing the properties of AlSi10Mg alloy fabricated by LPBF, achieving a balance between strength, elongation, and hardness.

5. Acknowledgments

This research was financially supported by the National Key R&D Program of China (Grant No. 2023YFB4604904).

6. References

1. Zhang H, Zhu HH, Qi T, Hu Z, Zeng X. Selective laser melting of high strength Al-Cu-Mg alloys: processing, microstructure and mechanical properties. Mater Sci Eng A. 2016;656:47-54. http://doi.org/10.1016/j.msea.2015.12.101.
2. Chen R, Xu QY, Liu BC. Modelling investigation of precipitation kinetics and strengthening for needle/rod-shaped precipitates in Al-Mg-Si alloys. Chin Shu Hsueh Pao. 2016;52:987-99.
3. Heinz A, Haszler A, Keidel C, Moldenhauer S, Benedictus R, Miller WS. Recent development in aluminium alloys for aerospace applications. Mater Sci Eng A. 2000;280(1):102-7. http://doi.org/10.1016/S0921-5093(99)00674-7.
4. Wang JY, Yang HL, Liu ZL, Fan L, Yan W, Qiu D, et al. Compositional regulation in additive manufacturing of precipitation-hardening (CoCrNi) 94Ti3Al3 medium-entropy superalloy: cellular structure stabilization and strength enhancement. Compos, Part B Eng. 2024;281:111507. http://doi.org/10.1016/j.compositesb.2024.111570.
5. Lv F, Liang HX, Xie DQ, Mao Y, Wang C, Shen L, et al. On the role of laser in situ re-melting into pore elimination of Ti-6Al-4V components fabricated by selective laser melting. J Alloys Compd. 2021;854:156866. http://doi.org/10.1016/j.jallcom.2020.156866.
6. Fan HJ, Hu JY, Wang Y, Zhang H, Guo W, Li J, et al. A review of Laser Additive Manufacturing (LAM) aluminum alloys: methods, microstructures and mechanical properties. Opt Laser Technol. 2024;175:110722. http://doi.org/10.1016/j.optlastec.2024.110722.
7. Hu ZP, Liu Y, Wu J, Dong J, Ma Z, Liu Y. The simultaneous improvement of strength and ductility of the 93W-4.6Ni-2.4Fe prepared by additive manufacturing via optimizing sintering post-treatment. Addit Manuf. 2021;46:102216. http://doi.org/10.1016/j.addma.2021.102216.
8. Wang JY, Yang HL, Fu MW. An additively manufactured heat-resistant Al-12Si alloy via introducing stable eutectic engineering. Addit Manuf. 2024;95:104523. http://doi.org/10.1016/j.addma.2024.104523.
9. Harrison NJ, Todd L, Mumtaz K. Reduction of micro-cracking in nickel superalloys processed by Selective Laser Melting: A fundamental alloy design approach. Acta Mater. 2015;94:59-68. http://doi.org/10.1016/j.actamat.2015.04.035.
10. Haubrich J, Gussone J, Barriobero-Vila P, Kürnsteiner P, Jägle EA, Raabe D, et al. The role of lattice defects, element partitioning and intrinsic heat effects on the microstructure in selective laser melted Ti-6Al-4V. Acta Mater. 2019;167:136-48. http://doi.org/10.1016/j.actamat.2019.01.039.
11. Liu YJ, Li SJ, Wang HL, Hou WT, Hao YL, Yang R, et al. Microstructure, defects and mechanical behavior of beta-type titanium porous structures manufactured by electron beam melting and selective laser melting. Acta Mater. 2016;113:56-67. http://doi.org/10.1016/j.actamat.2016.04.029.
12. Thijs L, Verhaeghe F, Craeghs T, Humbeeck JV, Kruth J-P. A study of the microstructural evolution during selective laser melting of Ti-6Al-4V. Acta Mater. 2010;58(9):3303-12. http://doi.org/10.1016/j.actamat.2010.02.004.
13. Xu W, Brandt M, Sun S, Elambasseril J, Liu Q, Latham K, et al. Additive manufacturing of strong and ductile Ti-6Al-4V by selective laser melting via in situ martensite decomposition. Acta Mater. 2015;85:74-84. http://doi.org/10.1016/j.actamat.2014.11.028.
14. Nadammal N, Cabeza S, Mishurova T, Thiede T, Kromm A, Seyfert C, et al. Effect of hatch length on the development of microstructure, texture and residual stresses in selective laser melted superalloy Inconel 718. Mater Des. 2017;134:139-50. http://doi.org/10.1016/j.matdes.2017.08.049.
15. Garibaldi M, Ashcroft I, Simonelli M, Hague R. Metallurgy of high-silicon steel parts produced using selective laser melting. Acta Mater. 2016;110:207-16. http://doi.org/10.1016/j.actamat.2016.03.037.
16. Prashanth KG, Scudino S, Eckert J. Defining the tensile properties of Al-12Si parts produced by selective laser melting. Acta Mater. 2017;126:25-35. http://doi.org/10.1016/j.actamat.2016.12.044.
17. Suryawanshi J, Prashanth KG, Scudino S, Eckert J, Prakash O, Ramamurty U. Simultaneous enhancements of strength and toughness in an Al-12Si alloy synthesized using selective laser melting. Acta Mater. 2016;115:285-94. http://doi.org/10.1016/j.actamat.2016.06.009.
18. Li XP, Ji G, Chen Z, Addad A, Wu Y, Wang HW, et al. Selective laser melting of nano-TiB2 decorated AlSil0Mg alloy with high fracture strength and ductility. Acta Mater. 2017;129:183-93. http://doi.org/10.1016/j.actamat.2017.02.062.
19. Zhang XY, Huang T, Yang WX, Xiao R, Liu Z, Li L. Microstructure and mechanical properties of laser beam-welded AA2060 Al-Li alloy. J Mater Process Technol. 2016;237:301-8. http://doi.org/10.1016/j.jmatprotec.2016.06.021.
20. Rosenthal I, Stern A, Frage N. Microstructure and mechanical properties of AlSi10Mg parts produced by the laser beam additive manufacturing (AM) technology. Metallogr Microstruct Anal. 2014;3(6):448-53. http://doi.org/10.1007/s13632-014-0168-y.
21. Thijs L, Kempen K, Kruth JP, Van Humbeeck J. Fine-structured aluminium products with controllable texture by selective laser melting of pre-alloyed AlSi10Mg powder. Acta Mater. 2013;61(5):1809-19. http://doi.org/10.1016/j.actamat.2012.11.052.
22. Giovagnoli M, Tocci M, Fortini A, Merlin M, Ferroni M, Migliori A, et al. Effect of different heat-treatment routes on the impact properties of an additively manufactured AlSi10Mg alloy. Mater Sci Eng A. 2021;802:140671. http://doi.org/10.1016/j.msea.2020.140671.
23. Wen T, Li ZC, Wang JY, Luo Y, Yang F, Liu Z, et al. From crack-prone to crack-free: eliminating cracks in additively manufacturing of high-strength Mg2Si-modified Al-Mg-Si alloys. J Mater Sci Technol. 2025;204:276-91. http://doi.org/10.1016/j.jmst.2024.04.009.
24. Chen YM, Wang LZ, Feng ZX, Zhang W. Effects of heat treatment on microstructure and mechanical properties of SLMed Sc-modified AlSi10Mg alloy. Prog Nat Sci. 2021;31(5):714-21. http://doi.org/10.1016/j.pnsc.2021.08.003.
25. Girelli L, Tocci M, Conte M, Giovanardi R, Veronesi P, Gelfi M, et al. Effect of the T6 heat treatment on corrosion behavior of additive manufactured and gravity cast AlSi10Mg alloy. Materials and Corrosion-Werkstoffe und Korrosion. 2019;70(10):1808-16. http://doi.org/10.1002/maco.201910890.
26. Pirinu A, Primo T, Del Prete A, Panella FW, De Pascalis F. Mechanical behaviour of AlSi10Mg lattice structures manufactured by the selective laser melting (SLM). Int J Adv Manuf Technol. 2023;124(5-6):1651-80. http://doi.org/10.1007/s00170-022-10390-1.
27. Yu TY, Hyer H, Sohn YH, Bai Y, Wu D. Structure-property relationship in high strength and lightweight AlSi10Mg microlattices fabricated by selective laser melting. Mater Des. 2019;182:108062. http://doi.org/10.1016/j.matdes.2019.108062.
28. Yan Q, Song B, Shi YS. Comparative study of performance comparison of AlSi10Mg alloy prepared by selective laser

melting and casting. J Mater Sci Technol. 2020;41:199-208. http://doi.org/10.1016/j.jmst.2019.08.049.
29. Li DM, Qin RX, Xu JX, Chen B, Niu X. Effect of heat treatment on AlSi10Mg lattice structure manufactured by selective laser melting: microstructure evolution and compression properties. Mater Charact. 2022;187:111882. http://doi.org/10.1016/j.matchar.2022.111882.
30. Wang YX, Hao ML, Wang JL, Li M, Gu Z, Meng C, et al. Fabrication of diamond/AlSi10Mg composite using SLM: effects of processing parameters and pre-/post-treatments. J Manuf Process. 2023;95:27-37. http://doi.org/10.1016/j.jmapro.2023.04.001.
31. Tabatabaei N, Zarei-Hanzaki A, Moshiri A, Abedi HR. The effect of heat treatment on the room and high temperature mechanical properties of AlSi10Mg alloy fabricated by selective laser melting. J Mater Res Technol. 2023;23:6039-53. https://doi.org/10.1016/j.jmrt.2023.02.086.
32. Subramaniyan AK, Reddy AS, Mathias S, Shrivastava A, Raghupatruni P. Influence of post-processing techniques on the microstructure, properties and surface integrity of Al-Si-Mg alloy processed by laser powder bed fusion technique. Surf Coat Tech. 2021;425:127679. http://doi.org/10.1016/j.surfcoat.2021.127679.
33. Salmi A, Atzeni E, Iuliano L, Galati M. Experimental analysis of residual stresses on AlSi10Mg parts produced by means of selective laser melting (SLM). Procedia CIRP. 2017;62:458-63. http://doi.org/10.1016/j.procir.2016.06.030.
34. Gatto A, Cappelletti C, Defanti S, Fabbri F. The corrosion behaviour of additively manufactured AlSi10Mg parts compared to traditional Al alloys. Metals (Basel). 2023;13(5):913. http://doi.org/10.3390/met13050913.
35. Gu XH, Zhang JX, Fan XL, Zhang LC. Corrosion behavior of selective laser melted AlSi10Mg alloy in NaCl solution and its dependence on heat treatment. Chin Shu Hsueh Pao. 2020;33:327-37.
36. Shakil SI, Hadadzadeh A, Shalchi Amirkhiz B, Pirgazi H, Mohammadi M, Haghshenas M. Additive manufactured versus cast AlSi10Mg alloy: microstructure and micromechanics. Results in Materials. 2021;10:100178. http://doi.org/10.1016/j.rinma.2021.100178.
37. Van Cauwenbergh P, Samaee V, Thijs L, Nejezchlebová J, Sedlák P, Iveković A, et al. Unravelling the multi-scale structure-property relationship of laser powder bed fusion processed and heat-treated AlSi10Mg. Sci Rep. 2021;11(1):6423. http://doi.org/10.1038/s41598-021-85047-2. PMid:33742014.
38. Alghamdi F, Song X, Hadadzadeh A, Shalchi-Amirkhiz B, Mohammadi M, Haghshenas M. Post heat treatment of additive manufactured AlSi10Mg: on silicon morphology, texture and small-scale properties. Mater Sci Eng A. 2020;783:139296. http://doi.org/10.1016/j.msea.2020.139296.
39. Brandl E, Heckenberger U, Holzinger V, Buchbinder D. Additive manufactured AlSi10Mg samples using selective laser melting (SLM): Microstructure, high cycle fatigue, and fracture behavior. Mater Des. 2012;34:159-69. http://doi.org/10.1016/j.matdes.2011.07.067.
40. Biffi CA, Fiocchi J, Tuissi A. Selective laser melting of AlSi10Mg: Influence of process parameters on Mg_2Si precipitation and Si spheroidization. J Alloys Compd. 2018;755:100-7. http://doi.org/10.1016/j.jallcom.2018.04.298.
41. Takata N, Liu M, Kodaira H, Suzuki A, Kobashi M. Anomalous strengthening by supersaturated solid solutions of selectively laser melted Al-Si-based alloys. Addit Manuf. 2020;33:101152. http://doi.org/10.1016/j.addma.2020.101152.
42. Beeri O, Dunand DC, Seidman DN. Roles of impurities on precipitation kinetics of dilute Al-Sc alloys. Mater Sci Eng A. 2010;527(15):3501-9. http://doi.org/10.1016/j.msea.2010.02.027.
43. Kumar NMS. A critical review on heat treatment of aluminium alloys. Mater Today Proc. 2022;58:71-9. http://doi.org/10.1016/j.matpr.2021.12.586.
44. Liu XH, Zhao CC, Zhou X, Shen Z, Liu W. Microstructure of selective laser melted AlSi10Mg alloy. Mater Des. 2019;168:107677. http://doi.org/10.1016/j.matdes.2019.107677.
45. Wang JY, Yang FP, Yang HL, Zhang L, Zhang Y, Liu Z, et al. Effect of heat treatment on the microstructure and mechanical properties of an Al-5Mg2Si-2Mg alloy processed by laser powder bed fusion. J Alloys Compd. 2022;920:165944. http://doi.org/10.1016/j.jallcom.2022.165944.

Data Availability

The full dataset supporting the findings of this study is available upon request to the corresponding author – Peng Liu, liupeng1286@mail.com.